Supplementary Information for

Ozonolysis of α-phellandrene, Part 1, Gas- and particle-phase characterisation

Felix A. Mackenzie-Rae[1], Tengyu Liu[3,4,a], Wei Deng[2,3], Xinming Wang[2,3], Sandra M. Saunders[1], Fang Zheng[3,4], Yanli Zhang[2,3]

[1] *School of Chemistry and Biochemistry, The University of Western Australia, Crawley WA 6009, Australia*

[2]*Center for Excellence in Regional Atmospheric Environment, Institute of Urban Environment, Chinese Academy of Sciences, Xiamen 361021, China*

[3]*State Key Laboratory of Organic Geochemistry and Guangdong Key Laboratory of Environmental Protection and Resources Utilization, Guangzhou Institute of Geochemistry, Chinese Academy of Sciences, Guangzhou 510640, China*

[4]*University of Chinese Academy of Sciences, Beijing 100049, China*

[a]*Now at City University of Hong Kong*

S.1 α-phellandrene PTR-TOF Fragmentation

The fragmentation pattern of α-phellandrene upon protonation has been studied twice in the literature (Misztal et al. 2012; Tani, 2013), with fragmentation found to be significant. However both studies used a PTR-MS fitted with a quadrupole mass spectrometer. Transmission is known to be substantially different in the quadrupole and time-of-flight systems (Jordan et al., 2009), and so results are unlikely to directly translate into the PTR-TOF system.

The fragmentation pattern of α-phellandrene upon protonation in the PTR-TOF was investigated twice. Firstly the fragmentation pattern was determined by adding five aliquots of α-phellandrene to a clean chamber and observing the resultant PTR-TOF spectrum. Only those species that trace the parent ion across all five additions are considered α-phellandrene fragments. In the second test α-phellandrene was injected once, and the effect of changing the drift tube energy by varying the voltage was investigated.

To determine the fragments of α-phellandrene, the correlation coefficient of each ion with the parent α-phellandrene ion ($C_{10}H_{17}^+$) was determined. Results from the first experiment are plotted in Figure S.1.1. An empirical threshold of |R| = |0.9| is chosen to select potential fragment species. Other detected species are thought to be the result of background contaminants in the chamber.

Ions that fall above the selection threshold were plotted against the parent ion, with the gradient of linear fits determining the percentage contribution of the respective fragment relative to the parent ion. The contribution of a given ion to the total α-phellandrene signal is therefore given by:

$$F_i^+ = \frac{s_i}{\sum_i s_i} \times 100 \qquad \text{(S.1)}$$

where s_i is the slope of fragment 'i' and F_i^+ is the percentage contribution of fragment 'i' to the total α-phellandrene signal, with index 'i' run over all fragments satisfying |R| = |0.9|. Ions satisfying this condition for either experiment are listed in Tables S.1.1 and S.1.2, along with their contributions to the α-phellandrene signal.

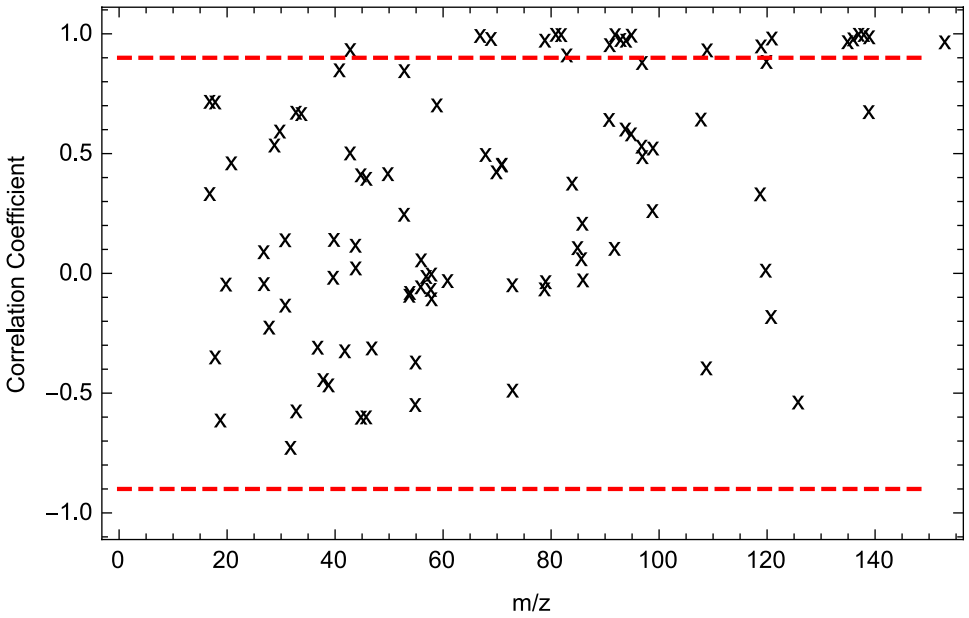

Figure S.1.1. Correlation coefficient for all ions with the α-phellandrene parent ion ($C_{10}H_{17}^+$) in the first calibration experiment. Dashed red lines denote correlation threshold.

Chemical ionisation of α-phellandrene in the PTR-TOF was found to produce 21 ions above a detection threshold of 5 cps. It is thought that the ion $C_9H_{13}O_2^+$ is produced by reaction with O_2^+ in the drift tube, leading to the loss of a CH_4 group. This process is only minor under the drift tube conditions investigated with all other fragments the result of conventional H_3O^+ protonation, confirming that O_2^+ reactions under the drift tube conditions employed are subsidiary to ionisation by H_3O^+. Nevertheless the PTR-TOF enables users to switch operation to an O_2^+ primary ion, with it thought that under this operating regime $C_9H_{13}O_2^+$ would be the major α-phellandrene fragment.

Mass (amu)	Ion	Correlation Coefficient	Percentage of total α-phellandrene signal (%)
43.06	$C_3H_7^+$	0.936	0.42 ± 0.02
67.10	$C_5H_7^+$	0.995	0.61 ± 0.01
69.12	$C_5H_9^+$	0.982	0.26 ± 0.007
79.10	$C_6H_7^+$	0.975	0.10 ± 0.003
81.11	$C_6H_9^+$	1.000	43.3 ± 0.3
82.18	$^{13}CC_5H_9^+$	0.999	2.60 ± 0.03
83.14	$C_6H_{11}^+$	0.914	0.11 ± 0.006
91.10	$C_7H_7^+$	0.957	0.20 ± 0.008
92.10	$C_7H_8^+$	0.999	1.14 ± 0.01
93.11	$C_7H_9^+$	0.979	10.2 ± 0.3
94.12	$^{13}CC_6H_9^+$	0.975	0.81 ± 0.03
95.13	$C_7H_{11}^+$	0.996	1.41 ± 0.02
109.13	$C_8H_{13}^+$	0.935	0.06 ± 0.003
119.12	$C_9H_{11}^+$	0.952	0.43 ± 0.02
121.13	$C_9H_{13}^+$	0.984	0.18 ± 0.005
135.15	$C_{10}H_{15}^+$	0.969	1.91 ± 0.07
136.19	$C_{10}H_{16}^+$, $^{13}CC_9H_{15}^+$	0.981	0.34 ± 0.01
137.20	$C_{10}H_{17}^+$	1.000	32.0 ± 0.2
138.17	$^{13}CC_9H_{17}^+$	0.999	3.28 ± 0.03

139.16	$^{13}C_2C_8H_{17}^+$	0.990	0.20 ± 0.004
153.15	$C_9H_{13}O_2^+$	0.969	0.42 ± 0.01

Table S.1.1. fragment ions of α-phellandrene from the first calibration experiment (E/N = 136 Td).

Mass (amu)	Percentage of total α-phellandrene signal (%)							
	E/N (Td)							
	149	137	130	121	111	102	92	83
81	42.3 ± 0.5	40.6 ± 0.4	39.9 ± 0.4	38.6 ± 0.5	36.1 ± 0.3	32.8 ± 0.3	28.2 ± 0.3	24.1 ± 0.3
82	2.72 ± 0.07	2.59 ± 0.07	2.54 ± 0.05	2.44 ± 0.06	2.29 ± 0.05	2.08 ± 0.06	1.82 ± 0.05	1.57 ± 0.04
92	2.06 ± 0.07	1.87 ± 0.05	1.81 ± 0.04	1.74 ± 0.05	1.70 ± 0.04	1.68 ± 0.05	1.69 ± 0.04	1.69 ± 0.05
93	18.7 ± 0.3	17.8 ± 0.2	17.2 ± 0.2	14.9 ± 0.2	11.3 ± 0.1	8.60 ± 0.1	7.25 ± 0.09	6.81 ± 0.09
94	1.53 ± 0.04	1.48 ± 0.04	1.42 ± 0.04	1.26 ± 0.04	0.98 ± 0.03	0.80 ± 0.03	0.71 ± 0.03	0.70 ± 0.03
95	2.76 ± 0.06	2.15 ± 0.05	1.96 ± 0.06	1.66 ± 0.05	1.43 ± 0.04	1.29 ± 0.04	1.19 ± 0.03	1.10 ± 0.03
119	1.56 ± 0.04	1.34 ± 0.04	1.25 ± 0.03	1.12 ± 0.03	1.05 ± 0.03	1.03 ± 0.02	1.03 ± 0.03	1.05 ± 0.03
135	2.31 ± 0.05	2.80 ± 0.05	3.24 ± 0.06	4.51 ± 0.1	6.73 ± 0.08	8.59 ± 0.08	9.87 ± 0.1	10.6 ± 0.1
137	22.8 ± 0.1	25.7 ± 0.2	26.9 ± 0.2	29.7 ± 0.2	33.7 ± 0.2	38.0 ± 0.2	42.3 ± 0.2	46.0 ± 0.2
138	2.49 ± 0.05	2.79 ± 0.05	2.90 ± 0.06	3.17 ± 0.06	3.58 ± 0.05	4.01 ± 0.06	4.46 ± 0.06	4.84 ± 0.07
153	0.72 ± 0.03	0.84 ± 0.04	0.90 ± 0.03	0.97 ± 0.02	1.09 ± 0.03	1.21 ± 0.03	1.40 ± 0.03	1.59 ± 0.04

Table S.1.2. Fragment ions of α-phellandrene at different drift tube energies as measured in the second calibration experiment.

The major signals observed in this work are the parent ion $C_{10}H_{17}^+$ and the fragments $C_6H_9^+$ and $C_7H_9^+$, consistent with the observations of Misztal et al. (2012) and Tani (2013). Indeed such a fragmentation pattern is common among monoterpenes. A similar distribution of minor fragments was observed in Misztal et al. (2012), although with slightly differing ratios. More ions were observed in first compared to the second calibration experiment, likely due to superior methodology of consecutive α-phellandrene additions. Based on the fragmentation pattern, a fragmentation scaling factor of 3.12 ± 0.02 and 2.96 ± 0.01 is used to correct the α-phellandrene parent signal (*m/z* 137) in experiments operating with the PTR-TOF drift tube set at E/N = 136 Td and E/N = 112 Td respectively. Nonetheless results suggest that molecules cannot effectively remove their excess energy through collisional thermalisation under the low pressures found in the PTR-TOF drift tube, with a large proportion fragmenting thus also expected for products.

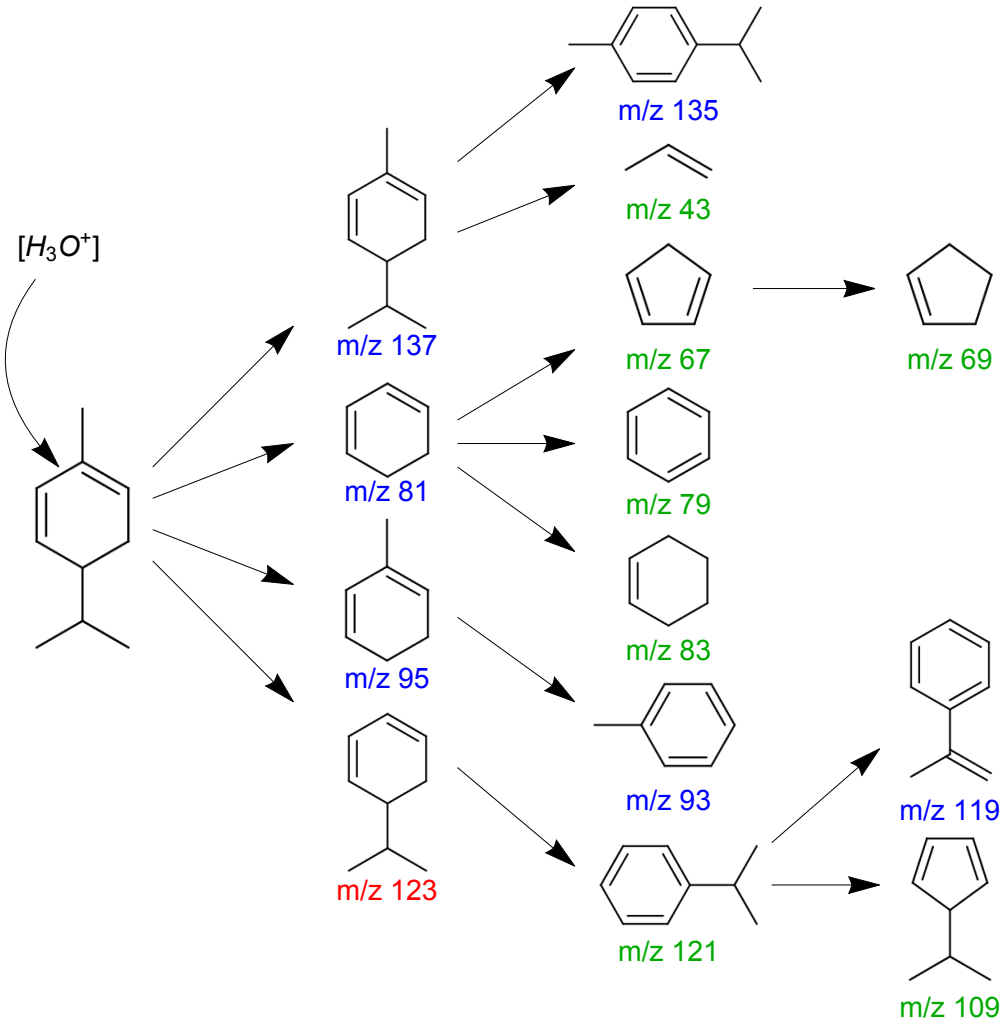

Figure S.1.2. Fragmentation of α-phellandrene in the PTR-TOF. The *m/z* values refer to the protonated fragments, not the neutral molecules as shown. Species that were identified as fragments in both calibration experiments are shown in blue, fragment species found only in first calibration experiment are green, while those that were not detected at the evaluation threshold in either calibration experiment are shown in red. Note that the structures of protonated fragment ions are unknown.

S.2 PTR-TOF Drift Tube Settings

The major ions from Table S.1.2 are plotted in Figure S.2.1. A similar study was conducted by sampling purified, dry air, and monitoring the concentration of primary ions. As expected water clusters, especially $(H_2O)_2^+$, became more influential as the drift tube voltage was lowered. A good compromise between α-

phellandrene fragmentation and water cluster formation was found to be 112 Td, which is marked by a pink line in the two figures. This setting was accordingly used in all subsequent experiments (numbers 8 – 11).

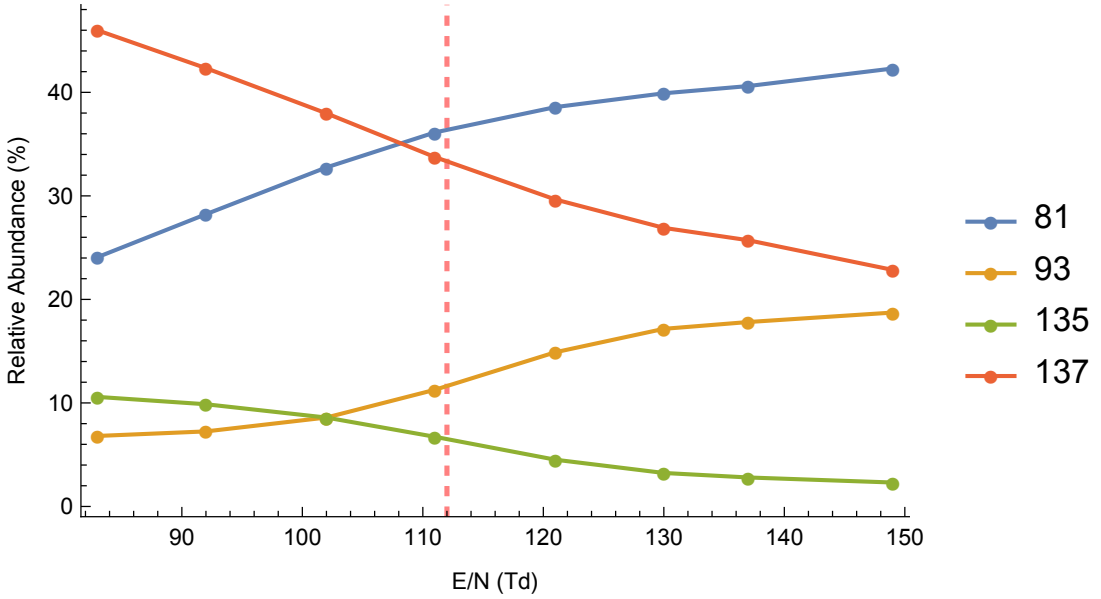

Figure S.2.1. Abundance of major fragment ions in the PTR-TOF at different drift tube energies.

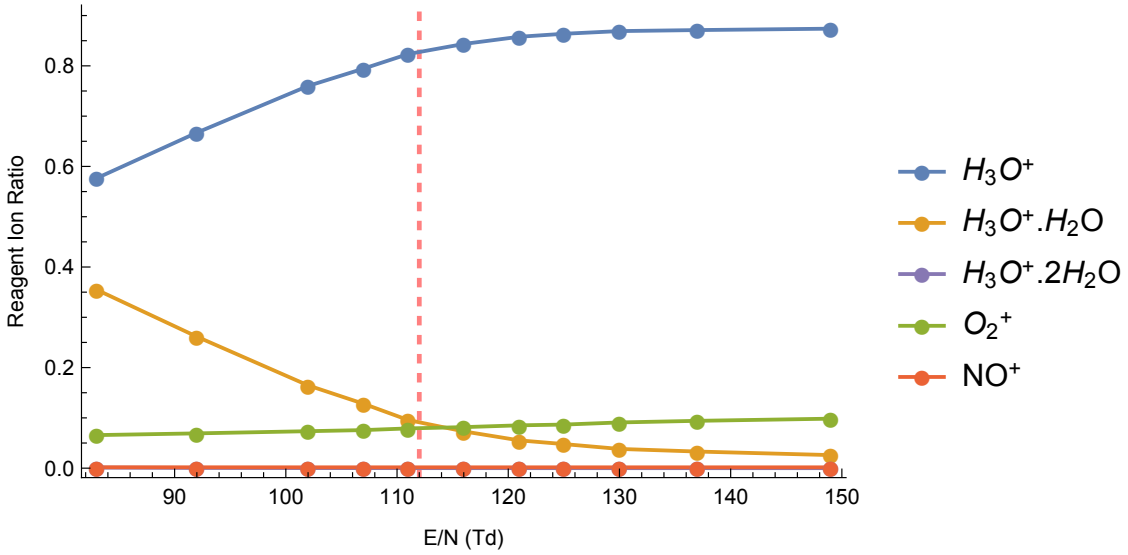

Figure S.2.2. Abundance of primary ions in the PTR-TOF at different drift tube energies.

S.3 Peaks *m/z* 167, 169, 185 – Dimers?

Signals at *m/z* 167, 169 and 185 are relatively invariant to ozone addition, lacking the characteristic rapid increase in concentration observed for other peaks upon ozone addition to the reactor (Figure S.3.1), suggesting that the

peaks might be formed by a process supplementary to direct ozonolysis. One possible candidate is product-product reactions, such as gas-phase accretion. To test the validity of this proposition, the simple model described in Section 3.1.3 of the main manuscript was extended by including the following code:

$$FG + FG \xrightarrow{k_4} DIMER$$

$$SG + SG \xrightarrow{k_5} DIMER$$

Results are plotted for Experiment 10, where the rate constants were set to $k_4 = k_5 = 3.0\text{x}10^{-19}$ cm^3 molecule^{-1} s^{-1} to achieve output on the same scale as the observed peaks. The model shows that a subsidiary process to the main ozonolysis scheme is capable of producing output similar to what is observed for *m/z* 167, 169 and 185 (Figure S.3.1), suggesting that the peaks may correspond to products of gas-phase accretion reactions. Their high molecular weights are suggestive of parent formulas such as $C_9H_{10}O_3$, $C_9H_{12}O_3$ and $C_9H_{12}O_4$ for *m/z* 167, 169 and 185 respectively. These formulas are consistent with first-generation products, although the peaks do not show the expected decay, whilst being too rich in carbon for expected second-generation products, whose formation is likely to be coupled with large parent fragmentation. It is therefore likely, although at this stage entirely speculative, that a process such as gas-phase accretion drives formation of the heavier species detected by the PTR-TOF in the ozonolysis of α-phellandrene.

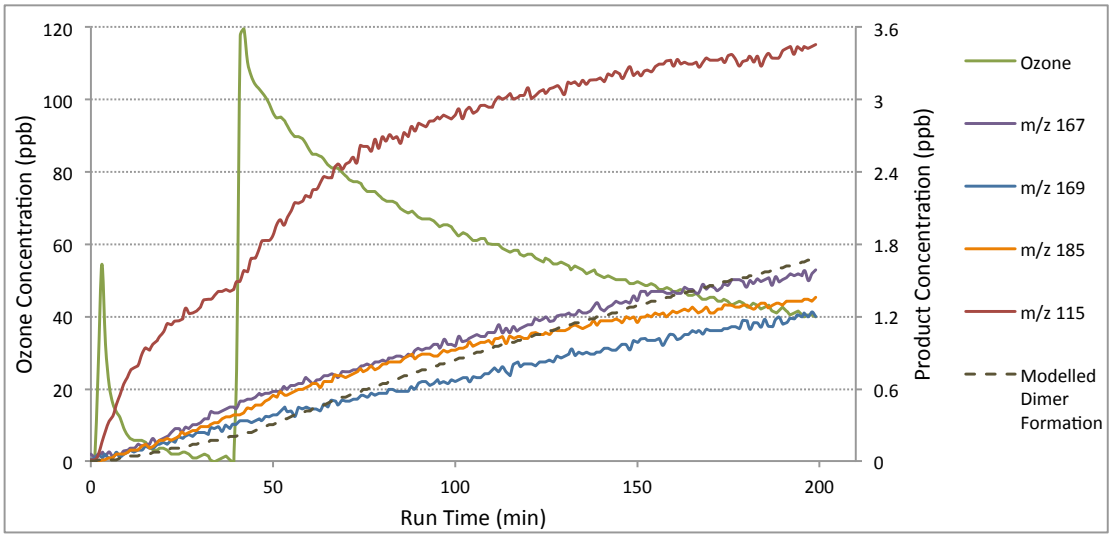

Figure S.3.1. Time profiles for ozone, a second-generation product (*m/z* 115) and peaks *m/z* 167, 169 and 185 in experiment 10, along with output from a simple dimer formation model.

S.4 α -phellandrene Degradation Mechanism

Addition of O_3 to the double bonds in α-phellandrene occurs through the well-established Criegee mechanism (Johnson and Marston, 2008), forming primary ozonides **POZ1** and **POZ2**. These structures can rapidly interconvert (Mackenzie-Rae et al., 2016), and decompose to yield four Criegee intermediates, **CI1**, **CI2**, **CI3** and **CI4**, as shown in Figures S.4.1 and S.4.2. The CIs, stabilised or chemically activated, can decompose through unimolecular processes as described in this supplementary entry, with thermalised CIs additionally able to partake in bimolecular reactions with available atmospheric species (Johnson and Marston, 2008; Vereecken and Francisco, 2012). The following discussion, though not exhaustive, does provide an overview of what are thought to be the most important pathways in the ozonolysis of α-phellandrene, leading to the second-generation product ions detected by the PTR-TOF.

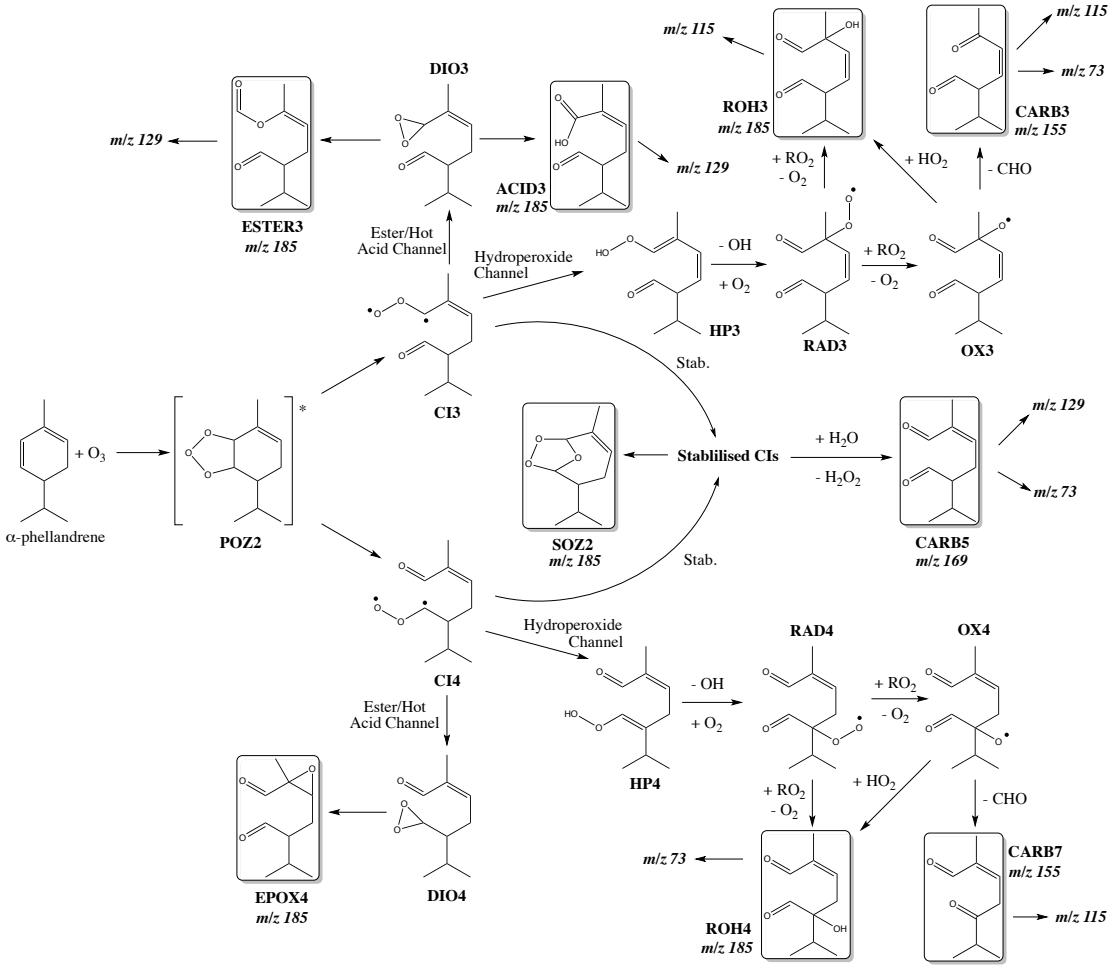

Figure S.4.1. Mechanism of O_3 addition to the more substituted double bond in α-phellandrene up to first-generation products. Species in boxes had ions of their corresponding mass detected by the PTR-TOF, with arrows showing detected masses correlating to products formed from a second ozonolysis.

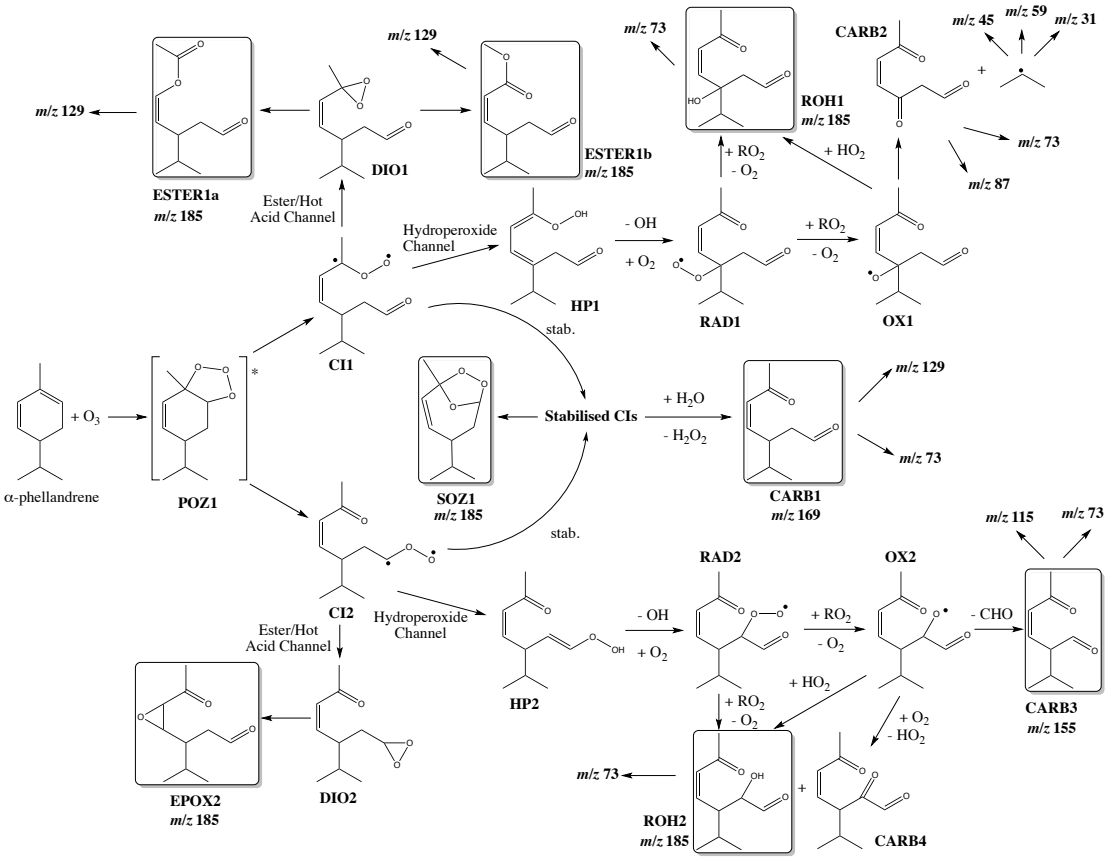

Figure S.4.2. Mechanism of O_3 addition to the less substituted double bond in α-phellandrene up to first-generation products. Species in boxes had ions of their corresponding mass detected by the PTR-TOF, with arrows showing detected masses correlating to products formed from a second ozonolysis.

S.4.1 Hydroperoxide Channel

Excited *syn*-CIs can access the hydroperoxide channel, whereby the CI rearranges via a *syn*-sigmatropic hydrogen shift into a vinyl hydroperoxide, before dissociating into an OH and alkyl radical (Johnson and Marston, 2008; Vereecken and Francisco, 2012). Further reactions of the alkyl radical lead to a range of multifunctional products. This channel is generally used to explain OH radical formation during alkene ozonolysis, with experimental OH yields suggesting it is

accessed approximately 35 ± 12% and 15 ± 7% of the time by α-phellandrene and its first-generation degradation products respectively.

Conventional thought is that the hydroperoxide channel proceeds through a 1,4-hydrogen shift (Johnson and Marston, 2008), with the mechanism shown for **CI2** and **CI4** in Figures S.4.1 and S.4.2, yielding **HP2** and **HP4**. Subsequent decomposition through OH loss follows, with an oxygen molecule adding to the 2-oxo-alkyl radicals yielding the peroxy radicals **RAD2** and **RAD4**. The peroxy radicals can react with other peroxy radicals or atmospheric species to give alkoxy radicals **OX2** and **OX4**, or react with other peroxy radicals in a disproportionation reaction to form α-hydroxycarbonyls (**ROH2**, **ROH4**) and α-dicarbonyls (**CARB4**). The alkoxy radicals formed from the hydroperoxide channel of **CI2** and **CI4** have a number of possible fragmentation and re-arrangement reactions however, given the presence of α-carbonyl groups, fragmentation into CHO and a dicarbonyl species (**CARB3**, **CARB7**) is thought to dominate (Jenkin et al., 1997; Vereecken and Peeters, 2009). The alkoxy radicals can also react with HO_2 to form the α-hydroxycarbonyls **ROH2** and **ROH4**, whilst **OX2** can also react with O_2 to produce **CARB4**.

Whilst a conventional 1,4-hydrogen shift is available in **CI1** by engaging the *syn*-methyl group, theoretical calculations showed an allyl-resonance stabilised 1,6-hydrogen shift to form **HP1** is exceedingly favoured (Mackenzie-Rae et al., 2016). An analogous channel forming **HP3** from **CI3** also exists, which is important, as conventional 1,4-hydrogen shifts are structurally unavailable in **CI3**. Upon loss of OH, electron density is spread over 3 carbons, providing multiple quasi-radical sites for oxygen addition. Theoretical calculations suggest all canonical structures contribute, with formation of the more stable tertiary peroxy radicals shown in Figures S.4.1 and S.4.2. After oxygen addition, resonance effects are no longer important, with the reaction mechanism proceeding as described for **CI2** and **CI4**. Decomposition of **OX3** yields the dicarbonyl **CARB3**. The major product expected from the decomposition of **OX1** is **CARB2**. Meanwhile the isopropyl radical can form acetone, acetaldehyde and formaldehyde, all of which are detected in large quantities in the PTR-TOF. Multiple fragmentation and re-

arrangement (e.g. 1,5-H shift) reactions are also possible for all radical species produced in the hydroperoxide channel of α-phellandrene CIs, with a plethora of products expected (Atkinson, 1997; Atkinson and Arey, 2003), the detail of which extends beyond the scope of the present study.

S.4.2 Ester or 'Hot' Acid Channel

Excited CIs can additionally re-arrange to form dioxiranes, although theoretical calculations show this to only be competitive for *anti*-conformers of **CI2**, **CI3** and **CI4** to form **DIO2**, **DIO3** and **DIO4** respectively (Mackenzie-Rae et al., 2016). Dioxiranes are known to rearrange to acids and esters (Vereecken and Francisco, 2012), with theoretical calculation showing re-arrangement of **DIO2** and **DIO4** to epoxides **EPOX2** and **EPOX4** is also possible. This reaction has precedence in the organic literature where dioxiranes are used as strong epoxidising agents (Murray, 1989). Epoxidation saturates the molecule, such that further reaction with ozone is unlikely. Nevertheless *m/z* 185 was not observed to increase rapidly upon commencement of the reaction indicating that epoxide formation is either of minor importance or lost during sampling and detection by the PTR-TOF like other first-generation products. For **DIO1** and **DIO3**, theoretical calculations show **ESTER1a** and **ESTER3** formation is favoured.

S.4.3 Stabilised CI Reactions

Excited POZs and CIs may be collisionally stabilised, yielding thermalised CIs. Theoretical calculations show the most favourable intramolecular reaction for thermalised α-phellandrene CIs is rearrangement into secondary ozonides (SOZs), forming **SOZ1** from **CI1** and **CI2**, and **SOZ2** from **CI3** and **CI4**. Rearrangement of **SOZ1** and **SOZ2** into acids and esters face large reaction barriers (Mackenzie-Rae et al., 2016), with the two SOZs likely to be thermalized and undergo a second reaction with ozone.

Intramolecular rearrangement occurs in competition with bimolecular reactions of CIs with available atmospheric species (e.g. HO, NO, SO, aldehydes, carboxylic acids). Inside the reactor thermalised CIs are most likely going to react with H_2O, forming dicarbonyls (**CARB1**, **CARB5**) or acids (**ACID2**, **ACID3**, **ACID4**)

(Atkinson, 1997). The acids formed are analogous to pinonic and limononic acids, which are important SOA constituents in the ozonolysis of α -pinine (Ma et al., 2007) and limonene (Leungsakul et al., 2005; Bateman et al., 2009).

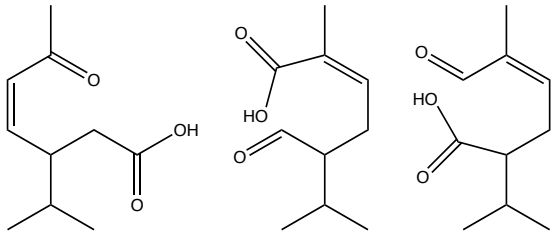

ACID2 **ACID3** **ACID4**

Figure S.4.3. First-generation acids formed from the reaction of water with stabilized CIs.

S.4.4 Reactions of First-Generation Products

Ozonolysis of α-phellandrene does not break the molecule as a whole. As a result first-generation products, in general, retain olefin functionality and are susceptible to further ozonolysis. The mechanistic channels available are similar to what has been described for α-phellandrene, although now POZ decomposition segments the molecule, forming pairs of products consisting of a CI and stable carbonyl species. An example of this is shown in Figure 6.

Figures S.4.1 and S.4.2 reference masses of products that are formed as direct carbonyl product from ozonolysis of first-generation products, which are also detected by the PTR-TOF. These include methyl glyoxal (*m/z* 73), which is formed from first-generation products **CARB1**, **CARB2**, **CARB3, CARB5**, **CARB7**, **ROH1**, **ROH2**, **ROH4**, **ACID2** and **ACID4**, 2-propan-2-ylbutanedial (*m/z* 129) which can be formed from **CARB1**, **CARB5**, **ESTER1a**, **ESTER1b**, **ESTER3** and **ACID3** and 2-propan-2-ylpropanedial (*m/z* 115) which is formed from **CARB3**, **CARB7** and **ROH3**. Analogous species can be formed with different functional groups according to parent species structure, although these are not detected by the PTR-TOF and are expected to be respectively minor.

Conversely CI fragments decompose similarly to the same pathways discussed for **CI1**, **CI2**, **CI3** and **CI4** resulting in a highly varied product distribution,

although for second-generation CIs intramolecular SOZ formation (when available) is unlikely to occur due to excessive ring strain (Chuong et al., 2004). Additionally the two novel channels discussed for α-phellandrene CIs, namely a 1,6-hydrogen shift and dioxirane epoxidation are no longer available pathways for the saturated second-generation products. Smaller CI products formed upon scission of the carbon backbone likely to lead to the production of the small species (< C_3) that dominate the measured gas-phase product distribution e.g. formaldehyde, acetaldehyde, formic acid and acetic acid. Additionally these smaller species are formed from fragments produced by radical-rearrangement and decomposition reactions that occur during gas-phase degradation e.g. glyoxal, acetone. Meanwhile participation of larger CI fragments formed from each of the first-generation products through the different possible mechanistic channels rapidly yields a large number of potential second-generation products expressing a variety of functionalities (Aumont et al., 2005). Detailing each of these products is out of the scope of the present study.

S.5 AMS Fragmentation Table

The default fragmentation table in the PIKA software was used, with modifications made to CO and H_2O fragmentation coefficients (Chen et al., 2011).

S.5.1 $(CO^+)_{org}$:$(CO_2^+)_{org}$

High-resolution analysis in the AMS is able to separate CO^+ and N_2^+ signals at *m/z* 28. Nevertheless the contribution particles make through CO^+ can be buried by the much larger N_2^+ signal from air, especially at low aerosol loadings. The fragmentation table therefore estimates the CO^+ organic component at *m/z* 28 using the organic component of the CO_2^+ signal at *m/z* 44, with a default scaling factor of 1.00 used based on the recommendation of Aiken et al. (2008). Nevertheless $(CO^+)_{org}$ can be quantitatively obtained by analysing experiments with sufficiently high M_{org} such that the AMS can accurately resolve the CO^+ and N_2^+ peaks. With this approach, four high M_{org} experiments were analysed yielded a $(CO^+)_{org}$:$(CO_2^+)_{org}$ ratio of 1.10 ± 0.13, which is used in the analysis of all low M_{org} experiments. The value is consistent with Chen et al. (2011), who found a

$(CO^+)_{org}$:$(CO_2^+)_{org}$ ratio of 1.08 ± 0.16 for aerosol generated from the ozonolysis of α-pinene.

S.5.2 $(H_2O^+)_{org}$:$(CO_2^+)_{org}$

The total signal intensity at *m/z* 18 contains contributions from molecular water (H_2O^+), atomic oxygen ($^{18}O^+$), ammonia ($^{15}NH_3^+$) and ammonium (NH_4^+). The latter two are resolved by the high-resolution spectra and so their impact can be ignored, while the air term ($^{18}O^+$) was shown to be minor by measuring particle free spectra. Sources of molecular water are water in the air (humidity), molecular water in the particles and water produced by the decomposition of particulate species.

To quantify the organic contribution of water aerosol was generated through the ozonolysis of α-phellandrene, before the humidity was gradually increased. Aerosol was given 1:15 hours to form, before humidity inside the reactor was changed from 10% to 95% over the next 3.5 hours. Throughout this time the AMS sample stream was periodically diverted so that it passed through an in-line HEPA capture filter (TSI). This created two sets of data, namely those with and those without particles.

The only source contribution to the *m/z* 18 signal when the HEPA filter is active is humidity. The default setting in the fragmentation table has, frag_RH = 0.01*frag_air[28], i.e. it is a expressed as a ratio of the measured signal for $(N_2^+)_{air}$. Plotting $(H_2O^+)_{humidity}$:$(N_2^+)_{air}$ against RH yields a line with slope (2.75 ± 0.09) × 10^{-4}, as shown in Figure S.5.1. The figure shows the ratio of $(H_2O^+)_{humidity}$:$(N_2^+)_{air}$ at humidity's used in this study (2 – 5%) is much smaller than the default AMS setting. Consequently when analysing the experimental data the following update is made, frag_RH = 0.0014*frag_air[28].

For the non-filtered data set, water can come from the gas- and particle-phase. The gas-phase contribution and molecular water existing inside the aerosol are both assumed to be zero at 0% RH, as all particle-phase water is assumed to

evaporate. Therefore, a plot of (H_2O^+) against RH yields the value of $(H_2O^+)_{org}$ at the y-intercept (0% RH), which was found to be 1.35 ± 0.06.

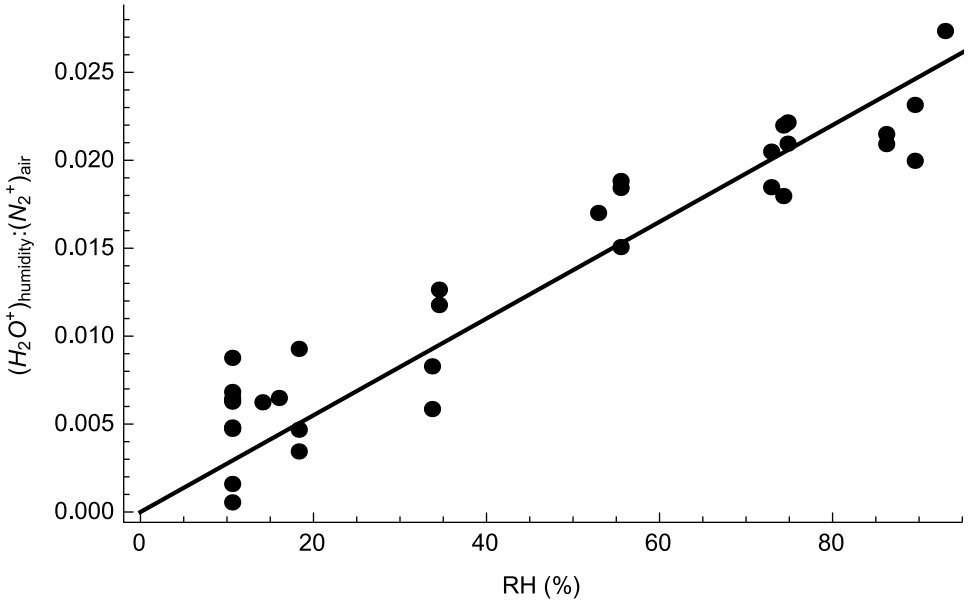

Figure S.5.1. Plot of $(H_2O^+)_{humidity}:(N_2^+)_{air}$ against RH for the HEPA filtered data set. Each dot corresponds to a V-mode measurement.

The fragmentation table defines frag_organic[18] = 0.225*frag_organic[44]. That is, it assumes the contribution water makes to the organic aerosol is 22.5% that of $(CO_2)_{org}$ (Aiken et al., 2008). The $(CO_2^+)_{org}$ signal is measured by the AMS, with the ratio of $[(H_2O^+)_{org}:(CO_2^+)_{org}]$ found to be 1.41 ± 0.09. Correcting for the differing relative ionisation efficiencies (RIE) of CO_2 (1.4, Alfarra et al., 2004) and H_2O (2, Mensah et al., 2011), a value of $[(H_2O^+)_{org}:(CO_2^+)_{org}]$ of 0.99 ± 0.06 is obtained. As noted by Chen et al. (2011), it is likely the multifunctional organic hydroperoxides prevalent in terpene ozonolysis results in a higher value than that proposed by Aiken et al. (2008). Meanwhile a value of 0.99 ± 0.06 is in excellent agreement with a value of 1 proposed in the original fragmentation table of Allan et al. (2004).

S.6 Comparison of SMPS and AMS Aerosol Mass Loadings

Wall loss rates calculated for density corrected SMPS and V-mode AMS data using the method of Pathak et al. (2007) are given in Table S.6.1. Minor differences are observed between experiments, however overall loss rates

measured by the two instruments correlate well. Determined loss rates were used to correct respective loading data.

No.	Wall Loss Rate (h^{-1})	
	SMPS	AMS
1	0.51 ± 0.01	0.550 ± 0.005
2	0.58 ± 0.02	0.51 ± 0.03
3	0.469 ± 0.007	0.482 ± 0.006
4	0.553 ± 0.004	0.520 ± 0.004
5	0.46 ± 0.01	0.539 ± 0.007
6	0.46 ± 0.01	0.55 ± 0.01
7	0.76 ± 0.02	0.72 ± 0.02
8	0.69 ± 0.01	0.72 ± 0.02
9	0.47 ± 0.01	0.525 ± 0.008
10	0.323 ± 0.007	0.326 ± 0.004
11	0.429 ± 0.006	0.479 ± 0.008

Table S.6.1. Aerosol wall loss rates measured by the SMPS and AMS for the α-phellandrene chamber ozonolysis experiments.

A scatter plot of total mass loading as measured by the SMPS and AMS, after correcting for wall losses, is shown in Figure S.6.1. The clustering of points around the 1:1 line indicates a general agreement between the two instruments, which is supportive of the assumption of spherical particles. The AMS systematically underrepresents aerosol yields under lower chamber mass loadings (< 100 μg m^{-3}) compared to the SMPS, which is indicative of a collection efficiency of less than unity. Under larger chamber loadings (>100 μg m^{-3}) data points are scattered either side of the 1:1 line. This is likely due to a cancellation of errors between the instruments, with larger particles that are cut off by the SMPS (d_m > 750 nm) becoming more influential. Without calibrating collection losses in the AMS, quantitative assessment remains speculative; nevertheless general agreement with the SMPS is observed.

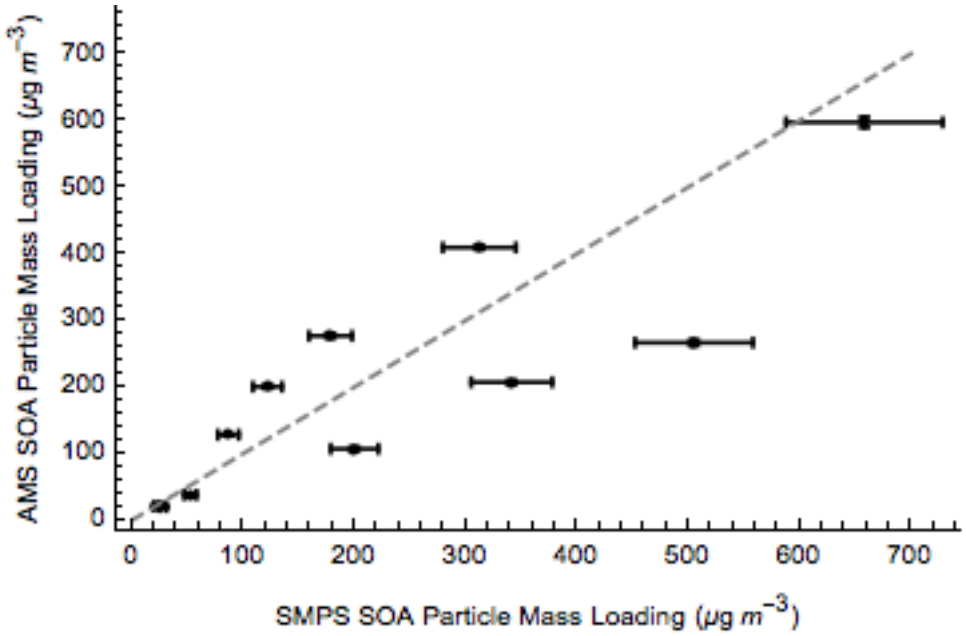

Figure S.6.1. SOA particle mass loading as measured by the AMS compared to those determined by density corrected SMPS volume loading data, with wall-losses corrected for. Dashed line is 1:1.

References

Aiken, A. C., Decarlo, P. F., Kroll, J. H., Worsnop, D. R., Huffman, J. A., Docherty, K. S., Ulbrich, I. M., Mohr, C., Kimmel, J. R., Sueper, D., Sun, Y., Zhang, Q., Trimborn, A., Northway, M., Ziemann, P. J., Canagaratna, M. R., Onasch, T. B., Alfarra, M. R., Prévôt, A. S. H., Dommen, J., Duplissy, J., Metzger, A., Baltensperger, U., Jimenez, J. L., 2008. O/C and OM/OC ratios of primary, secondary, and ambient organic aerosols with high-resolution time-of-flight aerosol mass spectrometry. Environ. Sci. Technol. 42, 4478–4485.

Alfarra, M. R., Coe, H., Allan, J. D., Bower, K. N., Boudries, H., Canagaratna, M. R., Jimenez, J. L., Jayne, J. T., Garforth, A. A., Li, S.-M., Worsnop, D. R., 2004. Characterization of urban and rural organic particulate in the Lower Fraser Valley using two Aerodyne aerosol mass spectrometers. Atmos. Environ. 38, 5745-5758.

Allan, J. D., Delia, A. E., Coe, H., Bower, K. N., Alfarra, R. M., Jimenez, J. L., Middlebrook, A. M., Drewnick, F., Onasch, T. B., Canagaratna, M. R., Jayne, J. T., Worsnop, D. R., 2004 A generalised method for the extraction of chemically

resolved mass spectra from Aerodyne aerosol mass spectrometer data. J. Aerosol Sci. 35, 909-922.

Atkinson, R., 1997 Gas-phase tropospheric chemistry of volatile organic compounds: 1. alkanes and alkenes. J. Phys. Chem. Ref. Data 26, 215-290.

Atkinson, R., Arey, J., 2003. Gas-phase tropospheric chemistry of biogenic volatile organic compounds: a review. Atmos. Environ. 37, S197-S219.

Aumont, B., Szopa, S., Madronich, S., 2005. Modelling the evolution of organic carbon during its gas-phase tropospheric oxidation: development of an explicit model based on a self generating approach. Atmos. Chem. Phys. 5, 2497-2517.

Bateman, A. P., Nizkorodov, S. A., Laskin, J., Laskin, A., 2009. Time-resolved molecular characterization of limonene/ozone aerosol using high-resolution electrospray ionization mass spectrometry. Phys. Chem. Chem. Phys. 11, 7931-7942.

Chen, Q., Liu, Y., Donahue, N. M., Shilling, J. E., Martin, S. T., 2011. Particle- phase chemistry of secondary organic material: Modeled compared to measured O:C and H:C Elemental ratios provide constraints. Environ. Sci. Technol. 45, 4763–4770.

Chuong, B., Zhang, J., Donahue, N. M., 2004. Cycloalkene ozonolysis: Collisionally mediated mechanistic branching. J. Am. Chem. Soc. 126, 12363-12373.

Jenkin, M. E., Saunders, S. M., Pilling, M. J., 1997. The tropospheric degradation of volatile organic compounds: A protocol for mechanism development. Atmos. Environ. 31, 81-104.

Johnson, D., Marston, G., 2008. The gas-phase ozonolysis of unsaturated volatile organic compounds in the troposphere. Chem. Soc. Rev. 37, 699-716.

Jordan, A., Haidacher, S., Hanel, G., Hartungen, E., Märk, L., Seehauser, H., Schottkowsky, R., Sulzer, P., Märk, T. D., 2009. A high resolution and high sensitivity proton-transfer-reaction time-of-flight mass spectrometer (PTR-TOF- MS). Int. J. Mass Spectrom. 286, 122–128.

Leungsakul, S., Jaoui, M., Kamens, R. M., 2005. Kinetic mechanism for predicting secondary organic aerosol formation from the reaction of d-limonene with ozone. Environ. Sci. Technol. 39, 9583-9594.

Ma, Y., Willcox, T. R., Russell, A. T., Marston, G., 2007. Pinic and pinonic acid formation in the reaction of ozone with α-pinene. Chem. Commun. 13, 1328-

1330.

Mackenzie-Rae, F. A., Karton, A., Saunders, S. M., 2016. Computational investigation into the gas-phase ozonolysis of the conjugated monoterpene α-phellandrene. Phys. Chem. Chem. Phys. 18, 27991-28002.

Mensah, A. A., Buchholz, A., Mentel, Th. F., Tillmann, R., Kiendler-Scharr, A. 2011. Aerosol mass spectrometric measurements of stable crystal hydrates of oxalates and inferred relative ionization efficiency of water. J. Aerosol Sci. 42, 11-19.

Misztal, P. K., Heal, M. R., Nemitz, E., Cape, J. N., 2012. Development of PTR-MS selectivity for structural isomers: Monoterpenes as a case study. Int. J. Mass Spectrom. 310, 10–19.

Murray, R. W., 1989. Dioxiranes. Chem. Rev. 89, 1187-1201.

Pathak, R. K., Stanier, C. O., Donahue, N. M., Pandis, S. N., 2007. Ozonolysis of α-pinene at atmospherically relevant concentrations: Temperature dependence of aerosol mass fractions (yields). J. Geophys. Res. 112, D03201.

Tani, A., 2013. Fragmentation and reaction rate constants of terpenoids determined by proton transfer reaction-mass spectrometry. Environ. Control Biol. 51, 23–29.

Vereecken, L., Francisco, J. S., 2012. Theoretical studies of atmospheric reaction mechanisms in the troposphere. Chem. Soc. Rev. 41, 6259-6293.

Vereecken, L., Peeters, J., 2009. Decomposition of substituted alkoxy radicals-part I: a generalized structure-activity relationship for reaction barrier heights. Phys. Chem. Chem. Phys. 11, 9062-9074.